# Simple reflection anisotropy microscopy set-up for CO oxidation studies

**C Punckt**[1,3]**, F S Merkt**[2] **and H H Rotermund**[1]

[1] Fritz-Haber-Institut der Max-Planck-Gesellschaft, Abteilung Physikalische Chemie, Faradayweg 4-6, D-14195 Berlin, Germany
[2] Universität Konstanz, Fachbereich Physik, Universitätsstr. 10, D-78457 Konstanz, Germany
Email: punckt@fhi-berlin.mpg.de

**Abstract.** Reflection anisotropy microscopy (RAM) is a tool to monitor the optical anisotropy of surfaces with spatial resolution (Rotermund *et al* 1995 *Science* **270** 608–10). It has been applied to pattern formation during CO oxidation on Pt(110), where it provides a high sensitivity for surface reconstruction and partially also for the coverage with reaction educts (Heumann 2000 *Dissertation* TU-Berlin). However, the spatial resolution of RAM and the alignment procedure of the optical components were not satisfactory. Here, we give a detailed description of a new set-up, which employs a simple polarizing beam splitter cube as an analyser instead of a Foster prism, offering a higher spatial resolution ($<10$ $\mu$m) and easier alignment of the optical components while retaining the high sensitivity for surface structure. Polarization contrast and spatial resolution of the new set-up are systematically measured, and applications to CO oxidation on uniform and microstructured Pt(110) single crystals are presented.

[3] Author to whom any correspondence should be addressed.

**IOP** Institute of Physics  **ⓘ** DEUTSCHE PHYSIKALISCHE GESELLSCHAFT

## Contents

## 1. Introduction

Optical techniques are of great importance for the analysis of surfaces, since they are non-invasive and applicable to any transparent working environment, like ultrahigh vacuum, high pressure systems or electrochemical experiments [1]–[7]. The study of optically anisotropic crystal surfaces was pioneered by Azzam [8] who used generalized ellipsometry to examine, e.g., calcite crystals. Later he developed the first normal incidence ellipsometer for the determination of the optical properties of uniaxial and biaxial bare and film-covered surfaces [9]. With the development of specialized optical components (photoelastic modulators (PEMs)), reflectance anisotropy spectroscopy (RAS), also called reflection difference spectroscopy (RDS), was born [1]. Amongst other techniques, it has been used to determine surface atomic and electronic structure [4, 10], it was applied to semiconductor surfaces, where it was employed as *in situ* monitor of thin-film epitaxial growth [1], [11]–[13], and to solid–liquid interfaces [14] where surface phase transitions, step morphology and electronic surface states could be measured. Koopmans *et al* [15] constructed a scanning RAS apparatus that allowed for spatially resolved studies. For a review paper about RAS, the reader is referred to [7]. However, scanning methods are not applicable to dynamic processes forming spatiotemporal patterns which vary on timescales of less than a second.

An instrument combining reflection anisotropy contrast with optical imaging at an image acquisition rate of 25 images per second was developed in order to image pattern formation processes in heterogeneous catalysis [16]. This reflection anisotropy microscope (RAM), similarly to Azzam's first set-ups, consisted of an ellipsometer where a simple lens was introduced in the reflected light beam, which imaged the sample under investigation onto a CCD camera. The set-up was later improved by employing a Foster prism, that improved both the contrast and the variety of possible light sources [17, 28]. Now measurements under normal incidence could be performed. However, the spatial resolution was low, since the small dimensions of the prism caused a numerical aperture of less than 0.025, limiting the theoretical (diffraction-limited) resolution to 17 $\mu$m (not taking into account aberrations). Furthermore, the alignment of the optical components was difficult, since the CCD camera used for image recording was rotated around the optical axis at an angle of 45°.

In this article, we describe a substantial improvement of the RAM instrument resulting in a spatial resolution of better than $10\,\mu$m (measured), simpler alignment and lower costs of the optical components. In contrast to similar optical surface analytical tools, like ellipsomicroscopy (EMSI) [18], RAM is applicable to composite surfaces, e.g. platinum single crystal surfaces with amorphous titanium islands on top, where a signal from the added artificial structures is undesired. The new set-up enables us to perform CO oxidation experiments in parameter regimes which were up to now inaccessible using optical methods.

## 2. RAM

Optically anisotropic media have a dielectric tensor with nonzero elements outside its diagonal [19]. This means that the electronic excitation of the material depends on the direction of the electric field. Upon reflection under normal incidence at the surface of these media, one measures different reflectivity depending on the polarization of the incident light. The optical anisotropy of the surface is characterized by the difference of the refractive indices under polarization along the principal dielectric axes $r_x$ and $r_y$. The azimuthal angle $\alpha$ of the probing light is defined as the angle between the polarization vector and the optical axis of $r_x$. When polarized light is reflected at an optically anisotropic surface, the polarization can change. This change in polarization depends on the azimuthal angle and is zero for $\alpha = 0°$ and $90°$ and maximum for $\alpha = \pm 45°$.

Platinum single crystals have a cubic crystal structure and therefore the anisotropy of the bulk is negligible. However, at the (110) surface, the bulk symmetry is broken; the surface reconstructs in a $1 \times 2$ 'missing row' structure [20, 21]. This results in an optical anisotropy of the Pt(110) surface. With RAM, we are capable of detecting the light component that has an altered polarization after reflection. Since we focus on the imaging of the surface anisotropy during pattern formation, a quantitative analysis of the effect is disregarded.

### 2.1. Experimental set-up

The set-up of a reflection anisotropy microscope is similar to a classical ellipsometer in the polarizer-sample-analyser (PSA) configuration operated at an angle of incidence $\phi = 0$ (figure 1). The polarization of the incident light changes upon reflection at an anisotropic surface, and the component of light which has changed polarization is detected with an analyser. In figure 2, our new set-up is shown. Like in our previous work [17, 28], we use the light of an Ar$^+$ laser as a light source. Via a fibre optic cable the light is guided to the experiment, collimated by an aspherical lens and polarized by a Glan–Thompson prism. An anti-reflection coated polarizing beam splitter cube (B Halle, Berlin; edge length 30 mm) is the heart of our new set-up. Its dielectric layer reflects 99.9% of the perpendicularly polarized (s-polarized) light which comes from the Glan–Thompson prism towards the investigated surface. If the polarization of the incident light does not coincide with one of the principal dielectric axes of the sample, after reflection the light contains a component which is parallelly polarized (p-polarized) with respect to the dielectric layer of the beam splitter. The component of light with unchanged polarization is reflected by the beam splitter towards the light source. The changed component is transmitted and used for imaging the surface with 2.9-fold magnification on to the chip of a CCD camera using a single achromatic lens ($f = 140$ mm).
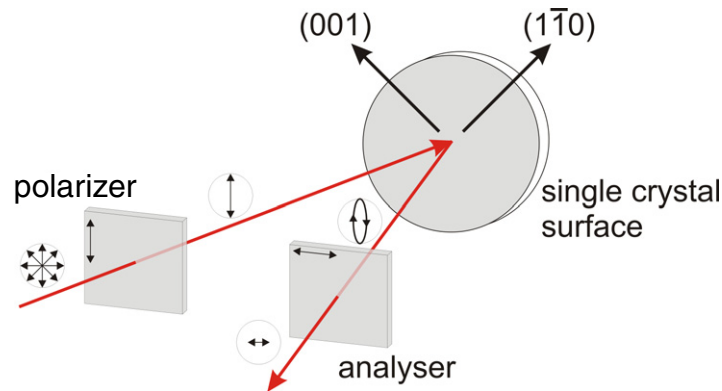
**Figure 1.** Principle of RAM. The circular symbols with arrows denote the polarization of light. For details see text.
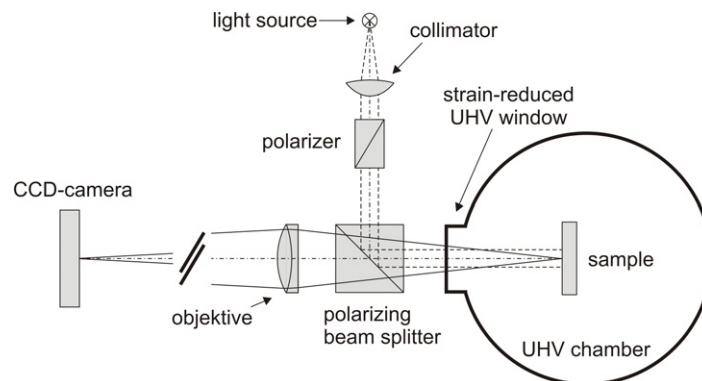


**Figure 2.** Experimental set-up.

Let $I_0$ denote the intensity of the probing light. Then the measured intensity of p-polarized light after reflection from a Pt(110) surface is on the order of $10^{-5}I_0$ [17, 28]. The beam splitter cube transmits a small fraction ($<0.04\%$) of s-polarized light. This means that the desired signal of $10^{-5}I_0$ is superimposed by a background intensity, which is one order of magnitude higher and therefore strongly affects the contrast. This drawback is met by a downstream real-time background subtraction and contrast enhancement of the video signal of the CCD camera using a Hamamatsu Argus 20 video processor. The images are stored on DVD at a rate of 25 images per second. Higher frame rates can be obtained using fast digital CCD cameras (cameras with frame rates up to 1000 images per second are commercially available).

The illumination optics, beam splitter cube, and imaging lens are mounted on to a rotary table (Owis) whose rotation axis coincides with the optical axis of the beam splitter and the imaging lens. Thus, the RAM set-up can be rotated and the azimuth angle varied while sample and camera remain in fixed positions. This greatly simplifies the adjustment of components and measurements at a given location on the sample under different azimuthal angles. The CO-oxidation experiments were performed using a Pt(110) single crystal which was located in an ultra high vacuum (UHV) chamber equipped with low energy electron diffraction (LEED), a quadrupole mass spectrometer (QMS) and computer-controlled gas dosing system. After polishing, the crystal was cleaned by repeated Ar ion sputtering, oxygen treatment and annealing at 900 K.
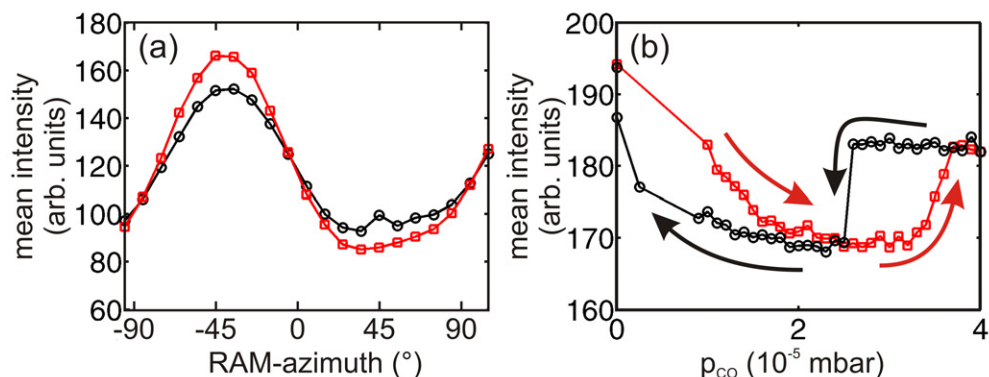
**Figure 3.** Polarization contrast with Pt(110). (a) Image intensity as a function of RAM azimuth. Red squares: oxygen-covered surface; black circles: reactive surface. Birefringence of the UHV window causes deformations of the curve. At an azimuthal angle of around $40°$, a contrast inversion takes place. (b) Image intensity as a function of CO partial pressure. Red squares: increasing $p_{CO}$ in steps of $0.1 \times 10^{-5}$ mbar every 5 s. Black circles: decreasing $p_{CO}$. For the whole measurement temperature and oxygen partial pressure were kept constant at $T = 478$ K and $p_{CO} = 2 \times 10^{-4}$ mbar.

## 2.2. Polarization contrast

A Pt(110) single crystal surface is in a $1 \times 2$ reconstructed state if exposed to oxygen or in vacuum. This reconstruction is lifted with increasing CO coverage. The transition starts at a CO coverage of around 0.2 ML and is completed at 0.5 ML [22, 23]. In order to examine the polarization properties of the new RAM set-up, the signal from a uniform Pt(110) surface both under oxygen-covered ($1 \times 2$ reconstructed surface) and reactive conditions (partly CO covered, reconstruction lifted) was measured at different azimuthal angles. Concerning the principle mechanism that provides the image contrast, our new set-up is identical with the old one. This means that also the dependence of image intensity on surface reconstruction and CO coverage is the same. With the old set-up it was found that the image intensity is mostly determined by the surface reconstruction and that the CO coverage only has a significant influence at high CO coverage [17]. This was proven by simultaneous measurements with RAM and LEED.

In figure 3(a) it is clearly seen that the oxygen-covered surface ($1 \times 2$ reconstructed) produces a larger variation of the mean image intensity than the reactive surface. Ideally, a sinusoidal shape should be obtained for both curves. Deviations likely stem from the contribution of the UHV window. At azimuthal angles of around $-45°$ and $45°$, maximal contrast is achieved. For the measurement shown in figure 3(b), the azimuth was fixed at $-45°$ and the CO partial pressure ($p_{CO}$) varied while keeping the partial pressure of oxygen ($p_{O_2}$) constant. When $p_{CO}$ is increased (red squares), the mean RAM intensity decreases and reaches a minimum at about $2.7 \times 10^{-5}$ mbar, where the reactivity of the catalytic surface is at its maximum. This means, that the highly reactive surface is predominantly deconstructed into a $1 \times 1$ missing row phase. A further increase of $p_{CO}$ leads to an increase of RAM intensity. The reaction stops and the surface is in a CO-poisoned state which is obviously less isotropic than the reactive state. If one decreases $p_{CO}$ (black circles), the surface remains in the poisoned state (hysteresis). At about

$2.5 \times 10^{-5}$ mbar, the reaction sets in again, and with decreasing reactivity (increasing oxygen coverage), the surface returns to its initial state. Here, another hysteresis effect can be observed. Similar observations were reported in a previous study with the old set-up [17]. The two curves would coincide, if the CO pressure was varied infinitely slowly. The mean image intensity of the fully CO-covered surface lies in-between the extremal values for the oxygen-covered and the reactive surface. This can be understood as a sensitivity for CO coverage. At intermediate coverages CO molecules are distributed rather randomly on the Pt surface and are adsorbed perpendicularly. When the CO coverage is increased, due to repulsive interactions CO molecules tend to arrange in an ordered way and show a tilt [24]. This may give rise to an increased anisotropy of the $1 \times 1$ CO-covered platinum surface compared to the $1 \times 1$ surface in the reactive state. The RAM intensities of the oxygen-covered surface and the reactive surface differ by about 10%. This is in good agreement with our estimation in the previous section, based on the polarization properties of the beam splitter. However, this would mean that the remaining anisotropy of the reactive surface, observed in figure 3(a) is solely caused by the UHV window. Whether this is really the case, or whether the beam splitter performs better than assumed cannot be decided from our measurements and should be analysed in future work.

To summarize, the contrast between the oxygen-covered and the reactive surface is caused by a change of the reconstruction of the Pt(110) surface, while the contrast between the reactive and the CO-covered (non-reactive) surface is provided by an influence of the adsorbed CO molecules. Both processes, the change of surface reconstruction, and the increase of CO coverage, are followed with RAM by detecting the effective overall optical anisotropy of the system. In the former case, the change of optical anisotropy is caused by surface reconstruction processes, while in the latter, the CO coverage induces an increase of anisotropy compared to the reactive surface.

### 2.3. Spatial resolution

The spatial resolution of our set-up was estimated by taking images of a well-defined object (Siemensstern) with incoherent non-polarized light and determining the approximate optical transfer function (OTF) $H(\omega_x, \omega_y)$ which is a complex function of the spatial frequencies in the object plane. Mathematically, $H$ can be defined as the Fourier transform of the point spread function (PSF) (the image of an ideal, point-like object), or—in terms of signal processing—as the Fourier transform of the (in this case two-dimensional) pulse response (see also [19]). The Siemensstern consists of a circular disc with alternating absorbing (metal) and transparent sectors (figure 4(a)). It is uniformly illuminated from the back. Varying the focus in a range which includes the 'optimal' focus (This range can be estimated with the naked eye.) with a $2048 \times 2048$ pixel digital 12-bit CCD camera, a series of images of the Siemensstern is taken and stored in a computer. Two different methods to obtain the approximate OTF are used.

1. Edge analysis: the image of a step from a dark to a bright sector is analysed: a cut perpendicular to the edge is compared to the ideal step-like cut through the edge of the object. The OTF can be directly estimated as the quotient of the cross-spectral density functions of the object intensity distribution (ideal step) and the image intensity distribution (measured). A separation of the OTF into amplitude and phase yields the modulation transfer function (MTF) and the phase transfer function (PTF). We are mainly interested in the MTF, since it allows for estimating the amount an object is blurred in the image. A MTF value of
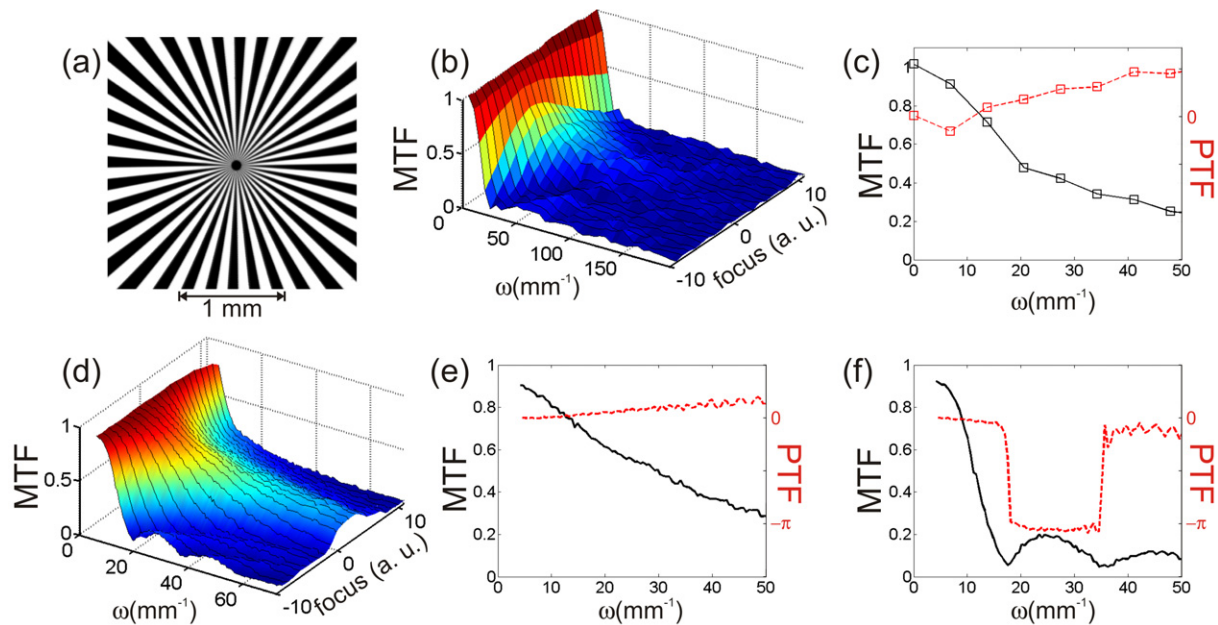
**Figure 4.** Evaluation of the approximate OTF (see text). (a) Test object (Siemensstern); (b) approximate MTF as a function of focus (edge analysis); (c) best MTF from (b) with corresponding PTF. (d) Approximate MTF as a function of focus (modulation analysis); (e) best MTF from (d) with corresponding PTF. (f) MTF and PTF at strong defocussing (from (d)). Between the spatial frequencies $\omega = 18\,\mathrm{mm}^{-1}$ and $\omega = 35\,\mathrm{mm}^{-1}$, the contrast is inverted (the real part of the OTF oscillates around zero).

0.5 at a certain spatial frequency means, for example, that the intensity modulation at this frequency is reduced by 50% in the image plane. MTFs at different foci of an image series are compared (figure 4(b)). The best focus is defined to be the one with the largest MTF value at a spatial frequency of 50 double lines per mm (50 mm$^{-1}$). The best-focus OTF for our system using edge analysis is shown in figure 4(c) separated into MTF and PTF. Using this method, the resolution in spatial frequency is low, but an analysis up to 200 mm$^{-1}$ is possible (depending on the size of the CCD pixels).

2. Modulation analysis: the modulation of the image intensity along concentric circular arcs is analysed for different radii. A cut through the image along a circular arc with large (small) radius corresponds to an object signal with low (high) spatial frequency. For the calculation of the OTF each circle is divided into 16 arcs, for each of which the analysis is performed individually. From the extreme values $I_{\mathrm{max}}$ and $I_{\mathrm{min}}$ of the image intensity along the arc, the modulation $M = (I_{\mathrm{max}} - I_{\mathrm{min}})/(I_{\mathrm{max}} + I_{\mathrm{min}})$ is determined. The phase can be estimated by fitting a sinus function to the intensity data and determining the phase shift of the fitted curve. The MTF as a function of the focus is plotted in figure 4(d), best-focus MTF and corresponding PTF using modulation analysis are shown in figure 4(e). This method is not accurate, because the intensity pattern in the object plane is not sinusoidal but step-like, and different frequencies are analysed at different object heights. However, it provides a high resolution in spatial frequency and it resolves the well-known contrast inversion at
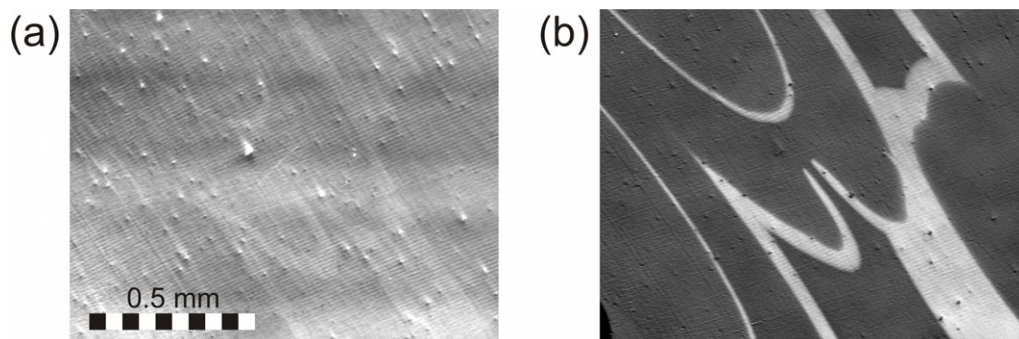
**Figure 5.** Concentration patterns (a) without and (b) with real-time background subtraction and contrast enhancement.

high spatial frequencies under strong defocussing (figure 4(f)) [19]. The maximum spatial frequency that can be analysed is limited by the structure size of the test object and has a value of about 100 mm$^{-1}$.

Depending on the method of analysis, the MTF at 50 mm$^{-1}$ has a value between 0.25 and 0.29 which is sufficient for imaging object structures with a size of less than 10 $\mu$m. The numerical aperture of our set-up is NA = 0.078 (due to a large working distance). For incoherent imaging this results in a theoretical resolution limit of $0.61\lambda/NA = 4\mu$m (after Abbe and Rayleigh) or 125 mm$^{-1}$, disregarding the aberrations caused by UHV window, beam splitter cube and lens. RAM measurements are performed using (partly) coherent imaging (illumination with NA $\approx$ 0). This increases the theoretical resolution limit to about 5 $\mu$m or 100 mm$^{-1}$ [19], which is an improvement by more than a factor of three compared to the old RAM. In contrast to set-ups employing Foster prisms, which are not available at sufficiently high aperture and lose their polarization properties already at NA > 0.1 (since their functionality is based upon total reflection), the resolution of our beam splitter set-up can still be improved using a larger NA because the extinction ratio between p- and s-polarized light only changes gradually with the angle of incidence at the dielectric layer. Also, polarizing beam splitter cubes are one order of magnitude cheaper than Foster prisms.

## 3. Application to CO oxidation

The new RAM set-up was used to study pattern formation during catalytic oxidation of CO on Pt(110). In figure 5(a), an example of propagating pulses of high CO coverage on a reactive surface is shown. The patterns are visible without electronic enhancement. The image quality can be substantially improved by downstream real-time background subtraction and contrast enhancement (figure 5(b)).

### 3.1. 'Memory effect'

Here we report on a novel observation, which we termed 'memory effect', recorded with RAM. It is illustrated in figure 6. On a reactive surface CO islands are grown for approx. 70 s (figure 6(a)) while CO and oxygen gases are both present at constant partial pressures in the reaction chamber.
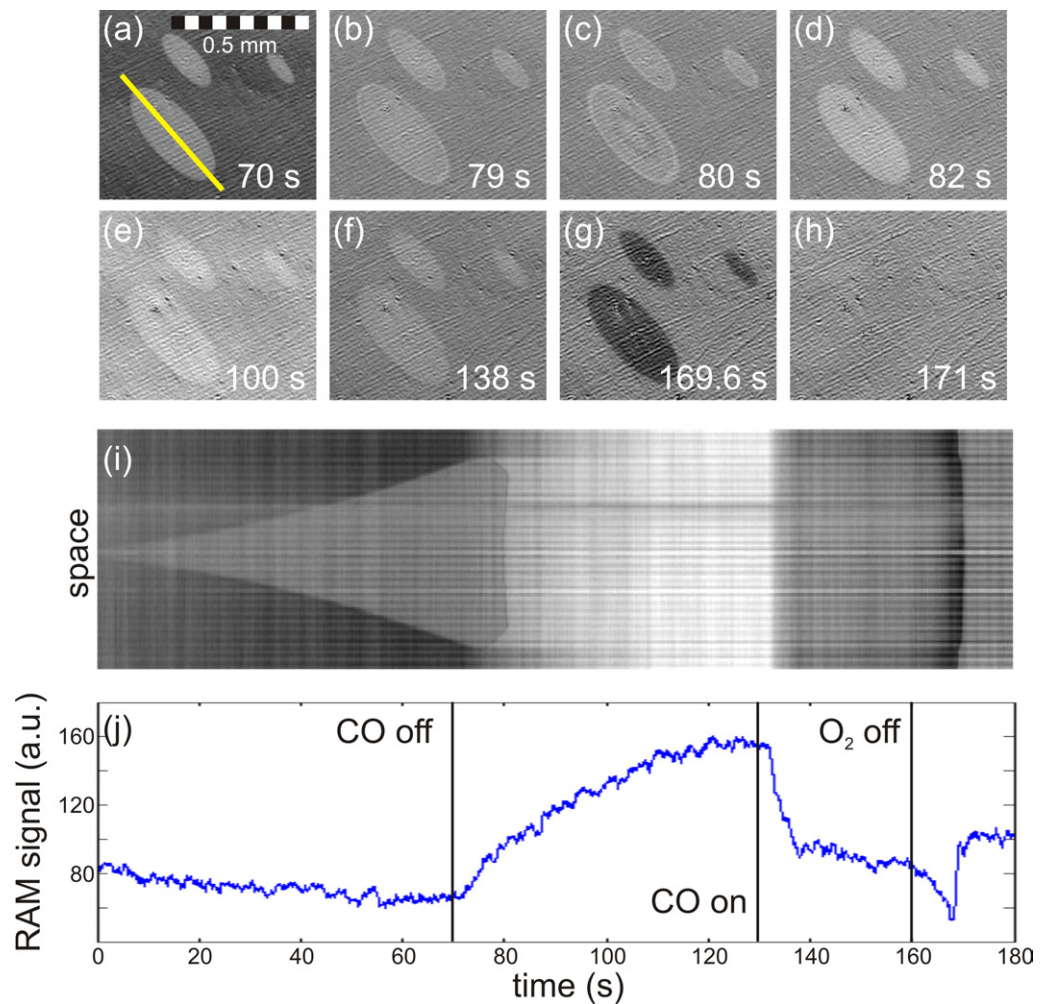
**Figure 6.** 'Memory effect'. (a–h) Snapshots of the surface at indicated times; (i) space–time plot along the line in (a); (j) mean RAM signal in a 10 by 10 pixel area at the bottom left of the images. Vertical lines indicate time moments of valve actions. $T = 439\,\text{K}$, $p_{O_2} = 2 \times 10^{-4}\,\text{mbar}$, $p_{CO} = 1.4 \times 10^{-5}\,\text{mbar}$.

At $t = 70\,\text{s}$ the CO valve is closed. Now the CO partial pressure is decreasing according to the pumping speed of our UHV system to a value well below $10^{-8}\,\text{mbar}$. With decreasing CO partial pressure, the CO coverage on the Pt surface decreases and outside of the CO islands a predominantly oxygen covered and therefore $1 \times 2$ reconstructed Pt surface establishes, thus increasing the image intensity slowly (figure 6(j)). The timescale of the intensity change is consequently determined by the CO pumping rate. The CO islands themselves are stable for approximately 9 s after CO is turned off. At $t = 79\,\text{s}$ (figure 6(b)), bright rings nucleate at the rims of the islands and expand slowly towards their centres. Only one second later, dark reactive zones nucleate at the centres of the islands (probably at the same surface defects where the CO islands initially had nucleated) and quickly propagate outwards as dark rings (figure 6(c)). After the inward- and outward-travelling rings have met at a position close to the boundaries of the islands, again homogeneous bright islands remain visible in the RAM image, although now the whole surface is reactive (figures 6(d) and (e)).

At $t = 130$ s, the bright islands are no longer visible, and the CO valve is opened again. The reactivity increases with increasing CO partial pressure within a few seconds. During this process, bright islands with exactly the shape of the original CO islands become visible (figure 6(f)). Obviously, the surface has a kind of 'memory' of the former islands. The structures disappear after about 2 s. Before new CO islands can nucleate on the surface, this time the oxygen valve is closed at $t = 160$ s. The RAM signal decreases everywhere on the surface for about 8 s, reaching a distinctive minimum when most of the oxygen atoms have been reactively desorbed leaving momentarily a highly reactive $1 \times 1$ reconstructed surface behind. Then the RAM intensity quickly jumps to an intermediate brightness which corresponds to the CO-poisoned surface (figure 6(h)). However, within the former CO islands this process is delayed by almost one second, and the original shapes of the islands reappear this time as dark areas for just a few seconds (figure 6(g)). The described dynamics can be seen in a space–time plot where for every video frame of the sequence a line profile along the white bar indicated in figure 6(a) is plotted against time (figure 6(i)). The space–time plots we display here always utilize full frames of the video as single time steps, which result inherently in a 40 ms time resolution. This is more easily seen with the enlarged time axis in figure 8(a), where around 20 s a fast wave starts. In principle, by using a faster CCD camera linked directly to a computer's RAM, a time resolution of 1 ms would be possible with our set-up. The polarization contrast is not affected hereby. However, the signal to noise ratio of the image sensor would be impaired when the time resolution was increased much further. This problem can be tackled simply by increasing the intensity of the illuminating laser, utilizing a pulsed laser, where high light intensities are confined in single nano- or even pico-second periods. Of course, then the data storage would become a serious problem. Generally, the set-up allows for analysis of much faster processes than the ones presented in this paper.

In order to verify that the observed slow timescale of the increase of the RAM signal after CO was turned off is due to the pumping rate of the system, we conducted an experiment where both CO and oxygen valves were closed simultaneously. The result is shown in figure 7. After the supply of reactants is turned off, the growth rate of the islands decreases, until the islands become almost stationary (figures 7(b) and (c)). During removal of reactants from the gas phase, the boundaries of the islands become somewhat fuzzy. This can be explained by diffusion of adsorbed CO. At $t = 186$ s the oxygen valve is opened and the oxygen pressure is increased to $2 \times 10^{-4}$ mbar within less than 3 s. Now the islands are reacted away homogeneously, and the RAM signal rapidly increases and reaches saturation after 15 s. Again, bright islands appear also on the oxygen covered surface (figure 7(d)). The timescale of the transition agrees quite well with LEED measurements of the surface reconstruction process at $T = 450$ K. At that temperature, about 10 s were needed to switch the surface from the $1 \times 1$ to the $1 \times 2$ state and vice versa, while at a temperature of about 500 K only a second is needed for this transition. However, a direct comparison of LEED and RAM signals is difficult, since atomic order on different lateral scales is measured.

To explore the temperature dependence of the memory effect, we repeated our experiments at different temperatures. At higher temperatures, the memory effect proceeds similarly (figure 8). No bright ring is observed, and the titration of the CO islands happens almost instantaneously (figure 8(d)). The approximate time needed to erase the islands during the oxygen covered state, such that they would not reappear after switching on CO, was measured. At $T = 491$ K, the islands did not reappear after switching off CO for 90 s. At 475 K (figure 8) the islands could still be observed after 240 s, and at 439 K (figures 6 and 7) the islands reappeared after more than
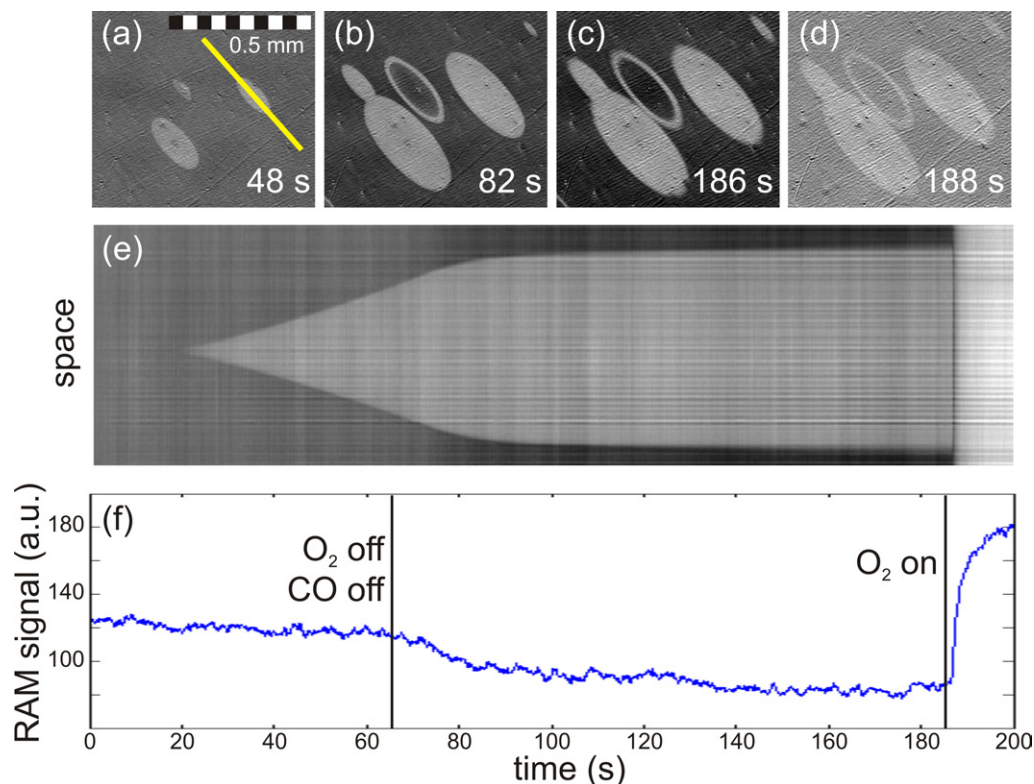
**Figure 7.** 'Memory effect'. (a–d) Snapshots of the surface at indicated times; (e) space–time plot along the line in (a); (f) mean RAM signal in a 10 by 10 pixel area at the bottom left of the images. Vertical lines indicate time moments of valve actions. $T = 439\,\text{K}$, $p_{O_2} = 2 \times 10^{-4}\,\text{mbar}$, $p_{CO} = 1.4 \times 10^{-5}\,\text{mbar}$.

10 min. Even after 12 min and repeated switching between the oxygen-covered and the reactive state, the islands could not be erased.

The following considerations might explain the 'memory effect'. Once a CO island has formed on the catalytic surface, at its location the platinum surface is in the $1 \times 1$ phase. When CO is turned off, the adsorbed molecules are reacted away by oxygen adsorbing from the gas phase. This first starts from the periphery of the islands. When CO reactively desorbs, it leaves a $1 \times 1$ surface behind, for which the sticking probability of oxygen is 50% increased compared to a $1 \times 2$ surface phase. Thus, the mean oxygen coverage on surface areas, which were formerly CO-covered, is increased for some time and the surface returns to the $1 \times 2$ reconstructed phase more rapidly, which locally increases the RAM signal. This explains the bright ring at the rim of the islands in figure 6(c) and the increased brightness of the whole island during the decrease of the CO pressure shown in figures 6(d) and (e).

We have therefore prepared two slightly different conditions for the following experimental procedure: when the CO valve is opened again, the sticking coefficient for oxygen is still slightly increased, which explains, why at the locations of the former CO islands a larger fraction of the surface stays in a $1 \times 2$ reconstructed state for some time. The difference decays over time, and the decay rate is temperature-dependent—the memory gets erased by annealing processes on the Pt surface. However, at sufficiently low temperature, the difference is large enough to have an effect also when oxygen is turned off after the reactive state was re-established (figure 6(g)).
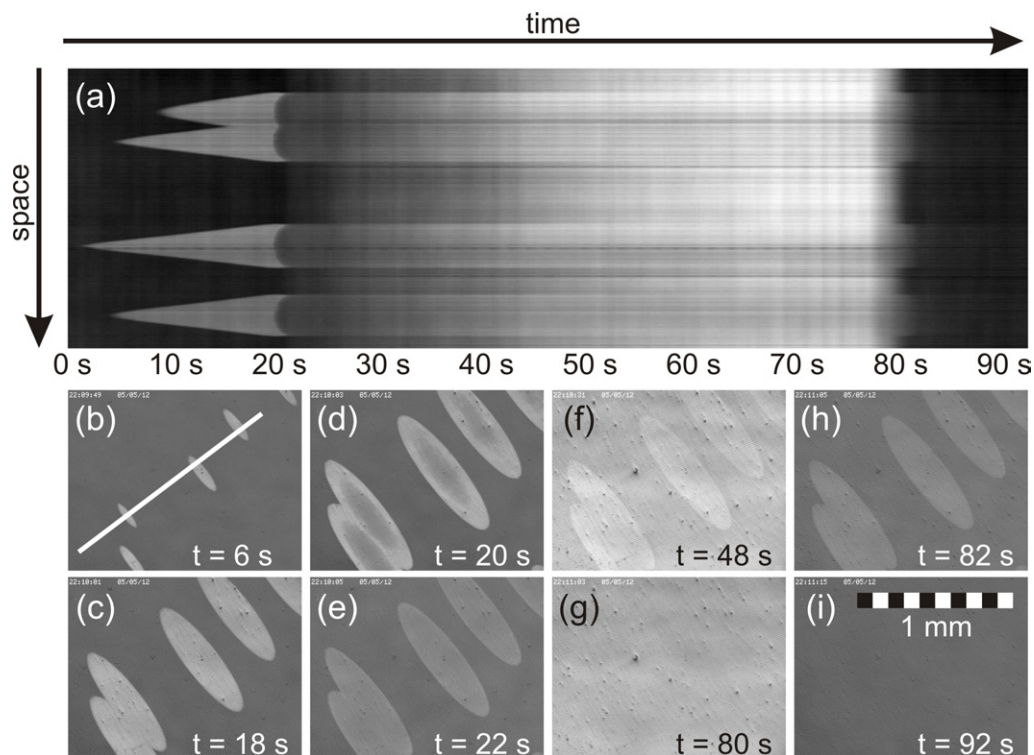
**Figure 8.** 'Memory effect'. (a) Space–time plot along the line in (b). (b–i) Snapshots of the surface at indicated times. $T = 475$ K, $p_{O_2} = 2 \times 10^{-4}$ mbar, $p_{CO} = 2.9 \times 10^{-5}$ mbar.

Earlier investigations utilizing a photoemission electron microscope (PEEM) described a similar 'memory effect' but for oxygen islands on a CO-covered Pt(100) surface [25]. There, the observation could be attributed to surface reconstruction processes, since the experiment was performed at temperatures below 360 K, where the change from the $1 \times 1$ to the $1 \times 2$ phase is known to proceed on a timescale of several minutes. At a slightly higher temperature of 373 K a similar result has been found utilizing EMSI [19], but there again it were oxygen islands which reappeared as shadows after being covered once more by CO.

Another PEEM study revealed similar island-shaped shadows during the formation of subsurface oxygen [26]. Oxygen atoms present on the catalytic surface can migrate below the first layer of Pt atoms when they are located on a $1 \times 1$ reconstructed surface. This process can only be observed after a special preparation technique. However, in our new experiments utilizing RAM, small amounts of subsurface oxygen might already be formed during the growth of the CO islands and might cause a detectable anisotropy of the surface. A more detailed analysis of the 'memory effect' will be the subject of future work.

## 3.2. Pulse propagation within microstructures

One advantage of RAM compared to ellipsometric imaging is the intrinsic insensitivity to amorphous (hence, isotropic) ad-layers on top of the catalytic surface. Together with its high spatial resolution, the new instrument now provides the possibility to analyse weak reaction pulses
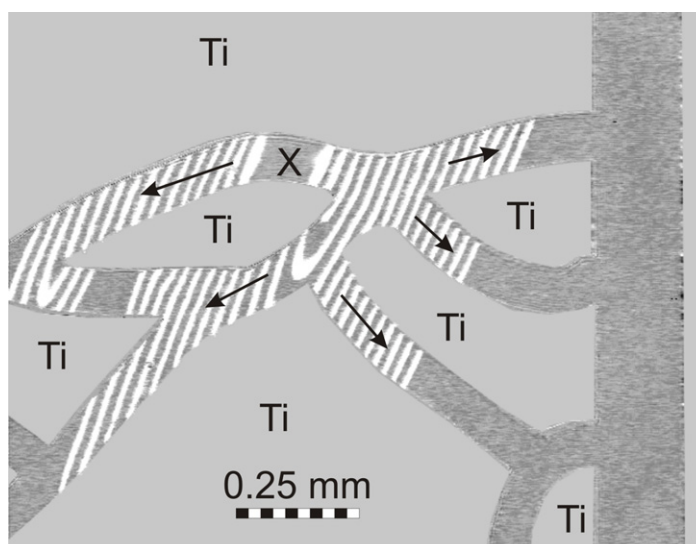
**Figure 9.** Combination of microstructures and surface addressing. Superimposed images of a single propagating pulse of high surface reactivity on a CO-poisoned background. The pulse was initialized with focussed laser light at the position indicated by 'X'. The arrows represent the pulse propagation direction.

propagating inside artificially created Ti microstructures [27], which has not been possible with the old set-up because of limited spatial resolution. Due to the large working distance (190 mm), the optical observation of concentration patterns could be combined with a spatiotemporal addressing of surface activity by means of focussed laser light. One example of a single propagating pulse in a 'river-delta' structure made by microlithography is shown in figure 9. The pulse was initiated on a completely CO-poisoned surface by shooting the laser light to the indicated position. The width of the Pt channels is $100\,\mu$m, and the approximate width of the propagating pulse is $15\,\mu$m. The image consists of a superposition of 15 snapshots of the surface that were taken at intervals of 3 s. Here, the RAM was adjusted to inverted contrast (see figure 3). The possibility to observe pattern formation combined with both microstructures and addressing paves the way for interesting new experimental approaches. This includes the systematic measurement of dispersion relation or behaviour in one-dimensional geometries under conditions where natural reaction patterns cease to appear and the dynamics have to be initiated artificially.

## 4. Conclusions

RAM is a powerful tool for analysing surface processes that involve changes in optical anisotropy. In addition to the UHV experiments shown here, it is applicable to a variety of different working environments like air or electrochemical systems. Polarization properties and spatial resolution of the set-up were determined, employing two simple methods to estimate the OTF of the imaging system. It provides a spatial resolution of better than $10\,\mu$m and employs simple optical components which are comparatively inexpensive and easy to align. Working under UHV conditions limits the resolution since a large working distance is necessary, but at the

same time allows for addressing of surface activity. Because of its insensitivity to artificial amorphous surface structures, pattern formation on microstructured catalysts could be observed, for the first time using focussed laser light to simultaneously generate and control surface activity. Employed in air, much shorter working distances (larger NA) are feasible and the resolution can be further increased. The time resolution of our set-up is limited by the frame rate of the CCD camera (here, 25 frames per second) and could easily be increased to 1 ms using commercially available fast digital CCD cameras. Finally, the new set-up could be a useful tool for material scientists analysing, e.g., polycrystalline samples, where different crystallites could be distinguished by different RAM intensity. Preliminary results obtained with the old RAM set-up using polycrystalline samples were reported in [17].

## Acknowledgment

## References

[1] Aspnes D E, Harbison J P, Studna A A and Florez L T 1988 Application of reflectance difference spectroscopy to molecular-beam epitaxy growth of GaAs and AlAs *J. Vac. Sci. Technol.* A **6** 1327–32

[2] Pidduck A J, Robbins D J, Cullis A G, Gasson D B and Glasper J L 1989 *In situ* laser-light scattering. 1. Detection of defects formed during silicon molecular-beam epitaxy *J. Electrochem. Soc.* **136** 3083–8

[3] Shen Y R 1989 Surface-properties probed by 2nd-harmonic and sum-frequency generation *Nature* **337** 519–25

[4] Kamiya I, Aspnes D E, Tanaka H, Florez L T, Harbison J P and Bhat R 1992 Surface science at atmospheric pressure—reconstructions on (001) GaAs in organometallic chemical vapor deposition *Phys. Rev. Lett.* **68** 627–30

[5] Rotermund H H 1997 Imaging of dynamic processes on surfaces by light *Surf. Sci. Rep.* **29** 267–364

[6] Punckt C, Bölscher M, Rotermund H H, Mikhailov A S, Organ L, Budiansky N, Scully J R and Hudson J L 2004 Sudden onset of pitting corrosion on stainless steel as a critical phenomenon *Science* **305** 1133–6

[7] Weightman P, Martin D S, Cole R J and Farrell T 2005 Reflection anisotropy spectroscopy *Rep. Prog. Phys.* **68** 1251–341

[8] Azzam R M A and Bashara N M 1974 Application of generalized ellipsometry to anisotropic crystals *J. Opt. Soc. Am.* **64** 128–33

[9] Azzam R M A 1977 Return-path ellipsometry and a novel normal-incidence null ellipsometer (NINE) *Opt. Acta* **24** 1039–49

[10] Baumberger F, Herrmann T, Kara A, Stolbov S, Esser N, Rahman T S, Osterwalder J, Richter W and Greber T 2003 Optical recognition of atomic steps on surfaces *Phys. Rev. Lett.* **90** 177402

[11] Richter W 1993 Optical *in-situ* surface control during MOVPE and MBE growth *Phil. Trans. R. Soc.* A **344** 453–66

[12] McGilp J F 1995 Optical characterization of semiconductor surfaces and interfaces *Prog. Surf. Sci.* **49** 1–106

[13] Zettler J T 1997 Characterization of epitaxial semiconductor growth by reflectance anisotropy spectroscopy and ellipsometry *Prog. Cryst. Growth Charact.* **35** 27–98

[14] Sheridan B, Martin D S, Power J R, Barrett S D, Smith C I, Lucas C A, Nichols R J and Weightman P 2000 Reflection anisotropy spectroscopy: a new probe for the solid-liquid interface *Phys. Rev. Lett.* **85** 4618–21

[15] Koopmans B, Richards B, Santos P, Eberl K and Cardona M 1996 In-plane optical anisotropy of GaAs/AlAs multiple quantum wells probed by microscopic reflectance difference spectroscopy *Appl. Phys. Lett.* **69** 782–4

[16] Rotermund H H, Haas G, Franz R U, Tromp R M and Ertl G 1995 Imaging pattern-formation in surface-reactions from ultrahigh-vacuum up to atmospheric pressures *Science* **270** 608–10

[17] Dicke J, Erichsen P, Wolff J and Rotermund H H 2000 Reflection anisotropy microscopy: improved set-up and applications to CO oxidation on platinum *Surf. Sci.* **462** 90–102

[18] Dicke J, Rotermund H H and Lauterbach J 2000 Ellipsomicroscopy for surface imaging: contrast mechanism, enhancement, and application to CO oxidation on Pt(110) *J. Opt. Soc. Am.* A **17** 135–41

[19] Born M and Wolf E 2005 *Principles of Optics* (Cambridge: Cambridge University Press)

[20] Jackman T E, Davies J A, Jackson D P, Unertl W N and Norton P R 1982 The Pt(110) phase-transitions: a study by Rutherford backscattering, nuclear microanalysis, LEED and thermal-desorption spectroscopy *Surf. Sci.* **120** 389–412

[21] Kellogg G L 1985 Direct observations of the $1 \times 2$ surface reconstruction on the Pt(110) plane *Phys. Rev. Lett.* **55** 2168–71

[22] Imbihl R, Ladas S and Ertl G 1988 The CO-induced $1 \times 1 \leftrightarrow 1 \times 2$ phase transition of Pt(110) studied by LEED and workfunction measurements *Surf. Sci.* **206** L903

[23] Gritsch T, Coulman D, Behm R J and Ertl G 1989 Mechanism of the CO-induced $1 \times 1 \leftrightarrow 1 \times 2$ structural transformation of Pt(110) *Phys. Rev. Lett.* **63** 1086–9

[24] Nowicki M, Emundts A, Pirug G and Bonzel H P 2001 CO adsorption on Pt(110) investigated by X-ray photoelectron diffraction *Surf. Sci.* **478** 180–92

[25] Rotermund H H 1999 Imaging surface reactions with a photoemission electron microscope *J. Electron Spectrosc.* **99** 41–54

[26] von Oertzen A, Mikhailov A S, Rotermund H H and Ertl G 1998 Subsurface oxygen in the CO oxidation reaction on Pt(110): experiments and modeling of pattern formation *J. Phys. Chem.* B **102** 4966–81

[27] Qiao L, Kevrekidis I G, Punckt C and Rotermund H H 2006 Guiding chemical pulses through geometry: Y junctions *Phys. Rev.* E **73** 036219

[28] Heumann J P 2000 Untersuchungen zur CO-Oxidation auf Platin mittels optischer Abbildungsmethoden *Dissertation* TU-Berlin